

Complexity of the laminar-turbulent boundary in pipe flow

Nazmi Burak Budanur^{1,2} and Björn Hof¹

¹*Nonlinear Dynamics and Turbulence Group, IST Austria, 3400 Klosterneuburg, Austria*

²*Kavli Institute for Theoretical Physics, UC Santa Barbara, Santa Barbara, CA 93106*

(Dated: December 14, 2024)

Over the past decade, the edge of chaos has proven to be a fruitful starting point for investigations of shear flows when the laminar base flow is linearly stable. Numerous computational studies of shear flows demonstrated the existence of states that separate laminar and turbulent regions of the state space. In addition, some studies determined invariant solutions that reside on this edge. In this paper, we study the unstable manifold of one such solution by the aid of symmetry-reduction and identify qualitatively different regions of the laminar-turbulent boundary. Upon our investigation, we discover a previously unknown traveling wave solution on the laminar-turbulent boundary with a relatively complex structure. By means of low-dimensional projections, we visualize different dynamical paths that connect these solutions to the turbulence. Our numerical experiments demonstrate that both solutions influence the asymptotic dynamics in the laminar-turbulent boundary.

PACS numbers: 02.20.-a, 05.45.-a, 05.45.Jn, 47.27.ed

I. INTRODUCTION

Pipe flow is the most prominent member of a class of canonical shear flows where transition to turbulence occurs despite the linear stability of the laminar state [1]. In the past two decades this problem enjoyed several major developments. The discovery of nonlinear traveling wave solutions [2–4] and studies [5–7] of the laminar-turbulent boundary began to elucidate the state space of the system using insights from dynamical systems theory.

In the dynamical systems approach to turbulence, fluid motion is envisioned as a trajectory in an infinite-dimensional state space [8]. For the case of shear flows with linearly stable laminar solutions, this state space accommodates a stable equilibrium point corresponding to the laminar solution and a chaotic set (an attractor or repeller) that is turbulence. Once this viewpoint is established, a natural question to ask is what separates these two distinct regions in the state space. In a small computational cell of channel flow, Itano and Toh [9] were first to study solutions that neither laminarize nor become turbulent using a shooting method and they discovered such trajectories tend towards a traveling wave solution. Following studies of shear flows in similar computational domains found periodic-like [10], equilibrium [11], as well as seemingly chaotic [5] solutions using similar shooting methods. These findings suggested the following picture of the state space of shear flows: The basin boundary between laminar and turbulent solutions is the stable manifold of an invariant set, whose unstable manifold on one side connects to the laminar solution and on the other side to the turbulent part of the state space. Schneider *et al.* [5] named this invariant set the “edge state”.

Schneider *et al.* [5] found in a short axially-periodic computational domain of pipe flow that the edge state exhibits chaotic motion, with flow structures much simpler than those of turbulence: a slow streak in the center surrounded by two fast streaks with chaotically moving streamwise vortices in between. A similar investigation in a long computational domain of pipe flow [7] yielded stream-wise localized edge states with chaotic dynamics, whose flow structures far away from the laminar interfaces resembled those computed in the short computational domain.

Typically when flows are not simplified by additional symmetries the edge state tends to be chaotic as is the case for plane Couette [12], channel [13], and asymptotic suction boundary layer [14] flows. In this seemingly generic case, the definition of the edge state is less clear than when it is formed by an exact invariant solution such as an (relative) equilibrium or a (relative) periodic orbit. In contrast to the invariant solutions, it is not straightforward to define and compute the stable/unstable manifolds of chaotic solutions, hence their theoretical study is much more challenging.

One way of systematically investigating chaotic edge states is studying the unstable invariant solutions that are contained within, since the geometry of chaotic sets are influenced by the invariant solutions that are embedded in them [15]. This strategy was adopted by Duguet *et al.* [6], who found for the case of pipe flow in an approximately 5-diameters long, axially periodic computational domain at $Re = 2875$ (Re based on bulk velocity and pipe diameter) that the chaotic edge state evolves around the “asymmetric” traveling wave solution found by Pringle and Kerswell [3]. In addition, they found a rotating traveling wave that had flow structures very similar to those of the asymmetric wave, but differently it rotated in the azimuthal direction in addition to drifting downstream.

Canonical shear flows (pipe, plane Couette, and plane Poiseuille) are symmetric under continuous translations in streamwise and spanwise directions. This implies that every generic (non-symmetric) solution of these systems have infinitely many copies that can be generated by symmetry transformations. We visualized this degeneracy on figure 1

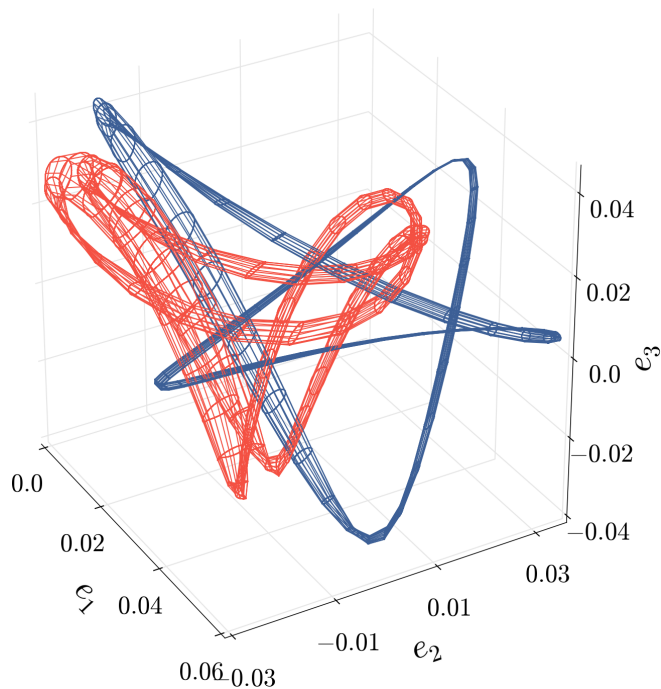


FIG. 1: Two traveling wave solutions of pipe flow (S1 and S1N, to be described later in the article) and their continuum of symmetry copies obtained from the streamwise translations and the azimuthal rotations, visualized as red and blue wire frames projected from the state space. Projection bases are the same with figure 4 and figure 5. Apparent intersections of the curves are the artifacts of finite-dimensional projection from the infinite-dimensional state space. In the symmetry-reduced state space, each torus will be represented by a single point.

for two traveling wave solutions we study in this article. Due to this multiplicity, something as simple as measuring the distance between two solutions becomes a daunting task. As a result, a common practice in dynamical systems approach to turbulence literature is to use quantities averaged over computational domains, such as energy input, dissipation, or pressure gradient, as indicators of “closeness” in the state space [14, 16–18]. While observing such quantities can be used for deciding if two solutions are far from each other, they cannot be used to conclusively decide if two solutions are close in the state space: Two solutions that have similar rates of energy input, dissipation, and pressure drop might have completely different flow structures. In this paper, this problem is addressed by symmetry reduction, for the first time in both axial and azimuthal directions of pipe flow. In the symmetry-reduced state space, the tori, such as those visualized on figure 1, are represented by single points, which simplifies the analysis substantially. As we will explain later in the article, our approach to this problem is generic and adaptable to other canonical shear flow geometries in a straightforward fashion.

For the application of our methods, we chose to revisit the laminar-turbulent boundary in a short (≈ 5 diameters) pipe flow at $Re = 3000$. To this end, we visualize numerical approximations to the unstable manifold of the asymmetric traveling wave that reside in the laminar-turbulent boundary on local projections akin to those pioneered by Gibson *et al.* [19]. We demonstrate that some parts of this unstable manifold that belong to the laminar-turbulent boundary exhibit dynamics qualitatively different from those previously attributed to the edge state in this setting. Upon further investigation, we discover that this region is in the vicinity of a previously unknown traveling wave solution with four high-speed streamwise streaks. This new traveling wave appears to belong to a higher-energy region in the edge state; closer to the turbulent part of the state space. We study the unstable manifold of the new traveling wave and demonstrate its different connections to the turbulence. Finally, we present the results of numerical experiments, which demonstrate that the trajectories on laminar-turbulent boundary of pipe flow transiently approach to the traveling waves that reside in the edge.

The rest of the paper is organized as follows. In the next section, we overview our methods, particularly in section II D, we present the generalization of the first Fourier mode slice [20] for simultaneous reduction of continuous symmetries in streamwise and spanwise directions. We present our results in section III, followed by the discussion in section IV.

II. METHODS

A. Numerical set-up

Numerical integration of the Navier–Stokes equations

$$\mathbf{u}_\tau + \mathbf{u}_{HP} \cdot \nabla \mathbf{u} + \mathbf{u} \cdot \nabla \mathbf{u}_{HP} + \mathbf{u} \cdot \nabla \mathbf{u} = -\nabla p + 32 \frac{\beta}{Re} \hat{\mathbf{z}} + \frac{1}{Re} \nabla^2 \mathbf{u}, \quad (1)$$

are performed using `Openpipeflow` [21]. The velocity field $\mathbf{u}(z, r, \theta; \tau)$ denotes the deviations from the base (Hagen–Poiseuille) solution $\mathbf{u}_{HP}(z, r, \theta) = 2(1 - (2r)^2)\hat{\mathbf{z}}$. Lengths and velocities are nondimensionalized by the pipe diameter D , and the mean axial speed U . Boundary conditions are no-slip and impermeable on pipe walls $\mathbf{u}(r = 1/2) = 0$; periodic in axial and azimuthal directions $\mathbf{u}(z, r, \theta) = \mathbf{u}(z + kL, r, \theta + m2\pi)$, $k, m \in \mathbb{Z}$. The velocity field satisfies the incompressibility condition $\nabla \cdot \mathbf{u} = 0$ and $\beta = \beta(\mathbf{u}(\tau))$ is a feedback term, adjusted in order to ensure a constant-flux equal to that of the laminar solution at a given Re . For all results of this paper, $Re = UD/\nu = 3000$; the pipe length is set to $L = \pi/0.625 \approx 5$; flow fields are discretized using $N = 128$ finite-difference points in radial direction and Fourier series truncated at $K = M = 64$ respectively in axial and azimuthal directions. Nonlinear terms are evaluated in the physical space on $(128 \times 192 \times 192)$ grid points following the 3/2-rule for dealiasing. This truncation yields more than 6×10^6 numerical degrees of freedom, which is significantly higher than the typical resolutions used in similar computational studies [5, 22]. Our choice yields at least 5 orders of magnitude drop in the spectral coefficients of the turbulent solutions at $Re = 3000$. While the solutions in the edge state generally require much less degrees of freedom to be resolved, we made this “conservative” choice since we investigate different regions of the edge state and we did not know a priori the maximum resolution requirement.

B. Symmetries

In this section, we review the symmetries of pipe flow and their representations in terms of their actions on the velocity field. For more detailed discussions of the symmetries and the invariant subspaces of pipe flow, we refer the reader to refs. [23, 24]. Pipe flow is equivariant under the streamwise translations $g_z(l)$, $l \in [0, L)$, the spanwise rotations $g_\theta(\phi)$ $\phi \in [0, 2\pi)$, and the reflection σ ; whose actions on the velocity field are given by

$$g_z(l)[u, v, w](z, r, \theta) = [u, v, w](z - l, r, \theta), \quad (2)$$

$$g_\theta(\phi)[u, v, w](z, r, \theta) = [u, v, w](z, r, \theta - \phi), \quad (3)$$

$$\sigma[u, v, w](z, r, \theta) = [u, v, -w](z, r, -\theta). \quad (4)$$

Therefore, the symmetry group of pipe flow is the direct product of $\text{SO}(2)_z$ and $\text{O}(2)_\theta$, i.e.

$$G = \text{SO}(2)_z \times \text{O}(2)_\theta = \{g_z(l), g_\theta(\phi), \sigma\}. \quad (5)$$

Lie group actions (2) and (3) can be written as operator-exponentials of their respective infinitesimal generators T_z and T_θ as

$$g_z(l) = e^{T_z l} \quad \text{and} \quad g_\theta(\phi) = e^{T_\theta \phi}, \quad (6)$$

where the actions of T_z and T_θ on the velocity field $\mathbf{u} = \mathbf{u}(z, r, \theta)$ are

$$T_z \mathbf{u} = -\frac{\partial}{\partial z} \mathbf{u} \quad \text{and} \quad T_\theta \mathbf{u} = -\frac{\partial}{\partial \theta} \mathbf{u}. \quad (7)$$

C. State space notation

Since we are going to use dynamical systems tools, it is handy to introduce a state space notation for use in the rest of the paper. Let $a(0)$ be a vector that contains all numerical degrees of freedom of a three-dimensional velocity field $\mathbf{u}(z, r, \theta; 0)$ at an initial time $\tau = 0$. Then, the Navier–Stokes equations (1) along with the incompressibility and the boundary conditions imply a finite-time flow

$$a(\tau) = f^\tau(a(0)), \quad (8)$$

where $a(\tau)$ corresponds to the velocity field $\mathbf{u}(z, r, \theta; \tau)$ at time τ . Assuming that the flow (8) is smooth, we can also represent the system as a high-dimensional ordinary differential equation

$$\dot{a} = v(a) = \lim_{\delta\tau \rightarrow 0} (f^{\delta\tau}(a) - a)/\delta\tau. \quad (9)$$

Actions of group elements $g \in G$ on a state space vector a should be thought as actions on the corresponding velocity fields as in (2-4). In other words, if a corresponds to velocity field \mathbf{u} then ga corresponds to the transformed velocity field $g\mathbf{u}$. Similarly, group tangents $t_{z,\theta}(a) = T_{z,\theta}a$ correspond to velocity fields $T_{z,\theta}\mathbf{u}$, where $T_{z,\theta}$ acts as in (7). In the state space, equivariance under g implies that state space velocity and finite-time flow commutes with g , i.e.

$$v(ga) = gv(a), \quad \text{and}, \quad f^\tau(ga) = gf^\tau(a). \quad (10)$$

Let a and a' correspond to velocity fields \mathbf{u} and \mathbf{u}' respectively, we define the inner product

$$\langle a, a' \rangle = \frac{1}{2} \int \mathbf{u} \cdot \mathbf{u}' dV, \quad (11)$$

where the integral is carried over the pipe volume. Thus, $\|a\|^2 = \langle a, a \rangle$ gives the kinetic energy of the velocity fluctuations; hence this choice of norm is usually referred to as the ‘‘energy norm’’.

D. Continuous symmetry reduction

We define the group orbit \mathcal{M}_a of a state-space point a as all points reachable from a by symmetry transformations, i.e.

$$\mathcal{M}_a = \{ga \mid g \in G\}. \quad (12)$$

If a is not invariant under any symmetries of the system, its group orbit (12) defines two distinct two-tori that are related to each other by the reflection σ since we have two compact continuous symmetry directions (5). All state-space points on a group orbit have the same physical properties, such as kinetic energy, dissipation, or wall-friction since these quantities are invariants of symmetry transformations. In addition, the dynamics of each point on a group orbit can be obtained from the dynamics of a single point following the definition (10) of equivariance. In other words, state-space of pipe flow exhibits a lot of redundancy since a generic point have infinitely many symmetry copies. Moreover, the presence of continuous symmetries renders the study of state space extremely hard: in the presence of pipe flow’s symmetries, measuring the distance between two generic state space points becomes the question of the minimum distance between tori, whose computational cost can easily become prohibitive if it is carried out at large numbers. *Continuous symmetry reduction*, which we introduce next, is a coordinate transformation such that state space points that are related by a continuous symmetries are represented by a single point in the reduced state space.

We begin by reducing the streamwise translation symmetry following [20] exactly: We define a ‘‘slice template’’ \hat{a}' with corresponding three-dimensional velocity field

$$[\hat{u}', \hat{v}', \hat{w}'](z, \theta, r) = J_0(\alpha r) \cos(2\pi z/L), \quad (13)$$

where J_0 is the Bessel function of the first kind, which vanishes at the pipe wall, i.e. $J_0(\alpha/2) = 0$. Then the translation symmetry-reduced coordinates are given by

$$\hat{a}(\tau) = g_z(L\phi_z/2\pi)a(\tau), \quad \text{where} \quad (14)$$

$$\phi_z(\tau) = \arg(\langle a(\tau), \hat{a}' \rangle + i \langle a(\tau), g_z(-L/4)\hat{a}' \rangle). \quad (15)$$

The transformation (14) exists as long as the phase (15) does. Note that ϕ_z is the polar angle when the state $a(\tau)$ is projected onto the plane spanned by $(\hat{a}', g_z(-L/4)\hat{a}')$.

Extension of (14) for the spanwise symmetry reduction is straightforward with a second slice template \tilde{a}' corresponding to the velocity field

$$[\hat{u}', \hat{v}', \hat{w}'](z, \theta, r) = J_0(\alpha r) \cos(\theta), \quad (16)$$

then the symmetry-reducing coordinate transformation becomes

$$\tilde{a}(\tau) = g_\theta(\phi_\theta)a(\tau), \quad \text{where} \quad (17)$$

$$\phi_\theta(\tau) = \arg(\langle \hat{a}(\tau), \tilde{a}' \rangle + i \langle \hat{a}(\tau), g_\theta(-\pi/2)\tilde{a}' \rangle). \quad (18)$$

Similar to (14) and (15), the transformation (17) exists as long as the phase (18) does. Our choice of the order at which the continuous symmetries are reduced is merely a convention since the inner products in (15) and (18) remain unchanged respectively under transformations (17) and (14). This is a result of the fact that streamwise translation and spanwise rotation symmetries commute; for a general symmetry group with non-commuting elements, a more careful treatment would have been required.

Budanur *et al.* [25] showed for a one-dimensional PDE with SO(2) symmetry that polar coordinate transformations similar to (14) and (17) can be reformulated as a “slice hyperplane”. A slice hyperplane is a set of points perpendicular to a slice template and is transversally intersected by the group orbits of the state-space points in the closed neighbourhood of the template. While a general slice has a finite region of applicability, if the template is chosen such that its dependence on the symmetry coordinate depends only on the first Fourier mode, then the slice works for a semi-infinite domain (half-hyperplane) that covers all state-space of interest, with a regularizable singularity in time. This method is named “first Fourier mode slice” in [25] and we refer the reader to [26] for a pedagogical introduction to it.

Reduced coordinates (14) satisfy the half-hyperplane equation

$$\langle \hat{a} - \hat{a}', t'_z \rangle, \quad \langle t_z(\hat{a}), t'_z \rangle > 0, \quad (19)$$

where $t_z(a) = T_z a$ is the group tangent of a state space point a and $t'_z = t_z(\hat{a}')$. Similarly, we can express the consequent transformation (17) as another half-hyperplane in the streamwise symmetry-reduced state-space as

$$\langle \tilde{a} - \tilde{a}', t'_\theta \rangle, \quad \langle t_\theta(\tilde{a}), t'_\theta \rangle > 0, \quad (20)$$

where similarly, $t_\theta(\hat{a}) = T_\theta(\hat{a})$ and $t'_\theta = t_\theta(\tilde{a}')$.

The main advantage of the reformulations (19) and (20) is that from this perspective one is able to derive projection operators for transforming the tangent space of a to the slice. Let δa be a small perturbation to a in the full state space, and ϕ_z be the slice phase that brings a to slice as $\hat{a} = g_z(\phi_z L/2\pi)a$, then the small perturbation can be brought to the slice by the projection

$$\delta \hat{a} = \left(1 - \frac{t_z(\hat{a}) \otimes t'_z}{\langle t_z(\hat{a}), t'_z \rangle} \right) g_z(\phi_z L/2\pi) \delta a \quad (21)$$

Similarly, $\delta \tilde{a}$ is transformed to the second slice (20) as

$$\delta \tilde{a} = \left(1 - \frac{t_\theta(\tilde{a}) \otimes t'_\theta}{\langle t_\theta(\tilde{a}), t'_\theta \rangle} \right) g_\theta(\phi_\theta) \delta \hat{a}, \quad (22)$$

where ϕ_θ is the slice-fixing phase (18), i.e. $\tilde{a} = g_\theta(\phi_\theta)\hat{a}$. For the derivation of these projection operators, we refer to the appendix of [20].

We are going to finish this section by explaining possible short-comings of the presented symmetry-reduction scheme: With the aid of the projections (21) and (22), it is straightforward to express state space velocity in the reduced state-space. Substituting δa with $v(a)$ in (21) we obtain

$$\begin{aligned} \hat{v}(\hat{a}) &= \left(1 - \frac{t_z(\hat{a}) \otimes t'_z}{\langle t_z(\hat{a}), t'_z \rangle} \right) g_z(\phi_z L/2\pi) v(a), \\ \hat{v}(\hat{a}) &= v(\hat{a}) - \frac{\langle t'_z, v(\hat{a}) \rangle}{\langle t_z(\hat{a}), t'_z \rangle} t_z(\hat{a}), \end{aligned} \quad (23)$$

where we used the first equivariance property in (10) and defined the stream-wise symmetry-reduced state-space velocity as $\hat{v}(\hat{a}) = \dot{\hat{a}}$. The fully symmetry-reduced state-space velocity $\tilde{v}(\tilde{a}) = \dot{\tilde{a}}$ can be similarly written as

$$\tilde{v}(\tilde{a}) = \hat{v}(\tilde{a}) - \frac{\langle t'_\theta, \hat{v}(\tilde{a}) \rangle}{\langle t_\theta(\tilde{a}), t'_\theta \rangle} t_\theta(\tilde{a}). \quad (24)$$

It is instructive to have a close look at (23): The reduced state space velocity \hat{v} is generated from full state space velocity v by subtracting the component in the direction of the group tangent with a pre-factor proportional to v 's projection onto the slice tangent. The second thing to recognize in (23) is the fact that $\langle t_z(\hat{a}), t'_z \rangle$ appears in the denominator, hence if this inner product vanishes, the reduced state space velocity field diverges. For a general slice, this condition sets the border in which the slice may apply [27, 28]; in our particular case of the first Fourier mode slice, this condition is equivalent to the existence of the phase (15). It can be shown [29] that the multipliers of group

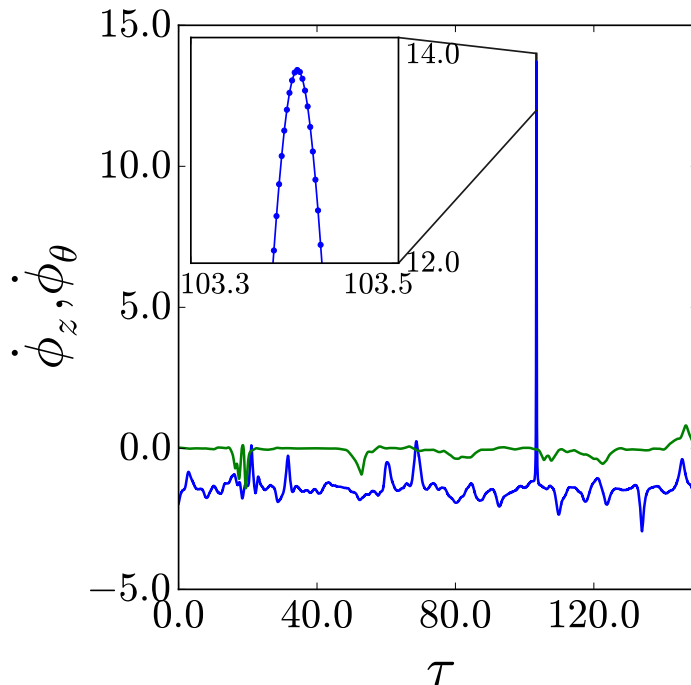


FIG. 2: Phase velocities (25) $\dot{\phi}_z$ (blue) and $\dot{\phi}_\theta$ (green) measured in a typical turbulence simulation. Inset: Zoom into the time interval $\tau \in [103.3, 103.5]$, where a sharp increase in $\dot{\phi}_z$ is apparent. Dots in the inset correspond to adjacent time-steps of the simulation, showing that this episode is in fact time-resolved.

tangents in (23) and (24) correspond to the time derivatives of the parameters of group actions that bring trajectories to the slice, i.e.

$$\dot{\phi}_z = \left(\frac{2\pi}{L} \right) \frac{\langle t'_z, v(\hat{a}) \rangle}{\langle t_z(\hat{a}), t'_z \rangle}, \quad \dot{\phi}_\theta = \frac{\langle t'_\theta, \hat{v}(\tilde{a}) \rangle}{\langle t_\theta(\tilde{a}), t'_\theta \rangle}. \quad (25)$$

Hence, these are appropriate quantities for checking whether or not the sliced dynamics is within its borders. Our experience with the first Fourier mode slices has been such that these quantities do not diverge for generic trajectories, although they may have “fast” episodes. We illustrate this for a typical turbulent trajectory in figure 2. Fast fluctuations that are caused by such episodes can be handled by rescaling the time-step of the numerical simulation or the problem can be explicitly reformulated using a “slice time” [25]. In this study, we found a fixed time-step $\Delta\tau = 0.0025$ to be sufficient to resolve the changes in slice phases, without resorting to an adaptive time-stepping scheme.

III. TRAVELING WAVES ON THE LAMINAR-TURBULENT BOUNDARY

Other than the laminar equilibrium, all invariant solutions such as traveling waves, rotating waves, relative periodic orbits, and possibly higher-dimensional invariant tori, of pipe flow drift downstream. A traveling wave a_{TW} is the simplest among those, which satisfies

$$a_{TW}(\tau) = g_z(c\tau)a_{TW}(0), \quad (26)$$

namely, its sole dynamics is a drift in the axial direction with constant phase speed c . Linear stability of this solution is described by the following eigenvalue problem [15, 30]

$$\left(\left. \frac{dv(a)}{da} \right|_{a=a_{TW}} - cT_z \right) V_i^{TW} = \lambda_i^{TW} V_i^{TW}, \quad (27)$$

where λ_i^{TW} and V_i^{TW} are the linear stability eigenvalues and eigenvectors respectively. Since the state space is formally infinite dimensional, each traveling wave has infinitely many stability eigenvalues and eigenvectors. In practice, we

solve (27) by Arnoldi iteration and approximate the finite-dimensional leading (most unstable) part of the tangent space.

Traveling waves become equilibria when the axial translation symmetry is reduced, say by the first Fourier mode slice method of (14). The translation symmetry-reduced state space still exhibits the $O(2)_\theta$ and it follows from the normal form analysis that all equilibria of an $O(2)$ -equivariant system belong to invariant subspaces of reflection symmetry or its conjugates [31]. Coming back to full state space, this implies that all traveling waves of pipe flow must be invariant under the reflection σ or a related symmetry. In particular, the solutions we are going to investigate in what follows are invariant under so-called shift-and-reflect symmetry

$$S = \sigma g_z(L/2) \in G. \quad (28)$$

In the shift-and-reflect subspace, continuous rotation symmetry (3) of the pipe flow is broken and only the discrete rotation by π is allowed [23]. Thus, the symmetry group of shift-and-reflect subspace is

$$G_S = \{g_z(l), g_\theta(\pi)\}. \quad (29)$$

Note that by definition, reflection symmetry is equivalent to an axial-translation by $L/2$.

A. Unstable manifold of S1

Numerical [6] and experimental [32] (combined with numerical work) evidence strongly suggests that the edge state of axially periodic pipe flow that is not long enough to exhibit streamwise localization is organized around the asymmetric traveling wave solution found in [3]. Following [4], we are going to refer to this solution as S1. This naming refers to solution's symmetries: S stands for 'shift-and-reflect' (28) invariance and 1 is the fundamental azimuthal wave number. S1 appears at a low- Re through a symmetry-breaking bifurcation of a $g_\theta(\pi)g_z(L/2)$ -symmetric solution, which itself is born out of a saddle-node bifurcation at even lower Re [3]. For the parameters studied here ($Re = 3000, L = \pi/0.625 \approx 5$) S1 and its two unstable eigenvectors with corresponding eigenvalues $\lambda_1^{S1} = \mu_1^{S1} = 0.0793, \lambda_2^{S1} = \mu_2^{S1} = 0.0223$ are visualized in figure 3. On figure 3 (a) and throughout the three-dimensional visualizations of this paper, streamwise velocity isosurfaces are chosen as 75% of their maximum/minimum values for velocity fluctuations. Similarly, vorticity isosurface levels are chosen at 60% of their respective maxima and minima. Numerical values of velocity/vorticity isosurfaces are given in the figure caption. For the two-dimensional cross-sectional visualizations of shift-and-reflect-symmetric states, we chose to average quantities over half pipe-length since the second half is simply the reflection of the first.

Duguet *et al.* [6] studied the evolution of perturbations along the unstable directions of S1. After confirming that the perturbations in $\pm V_1^{S1}$ direction either laminarizes or develops into turbulence, they focused on the perturbations on (V_1^{S1}, V_2^{S1}) plane that neither laminarize nor become turbulent. Running Newton searches near-recurrences of these trajectories, they found rotated versions of S1 and conjectured that S1's unstable manifold contains a "relative"-heteroclinic connection to its rotation by approximately 52° . This cannot be true since the unstable eigenvectors V_1^{S1} and V_2^{S1} are also shift-and-reflect symmetric, hence the associated unstable manifold lies in the shift-and-reflect invariant subspace, which only allows for azimuthal rotations by π . We are guessing that Duguet *et al.*'s conjecture was a result of a numerical error build up due to not restricting dynamics into the shift-and-reflect invariant subspace. Our first calculation in this paper will be very similar to theirs, with the symmetry-restriction requirement taken into account. In addition, we are going to carry out our computation in the translation symmetry-reduced state space (14), which will allow us to visualize the unstable manifold.

As a first approximation to S1's unstable manifold, we start trajectories with the initial conditions

$$\hat{a}_\phi(\tau = 0) = \hat{a}_{S1} + \epsilon \left(\frac{\hat{V}_1^{S1}}{\mu_1^{S1}} \cos \phi + \frac{\hat{V}_2^{S1}}{\mu_2^{S1}} \sin \phi \right), \quad (30)$$

where \hat{a}_{S1} is the symmetry-reduced state space point corresponding to S1, \hat{V}_1^{S1} and \hat{V}_2^{S1} are S1's leading linear stability eigenvectors projected onto the slice as described in (21), and $\epsilon = 10^{-4}$ is a small constant. (30) defines an ellipse on the $(\hat{V}_1^{S1}, \hat{V}_2^{S1})$ -hyperplane, parametrized by ϕ and the scaling of perturbations by corresponding eigenvalues $\mu_{1,2}^{S1}$ lets trajectories expand initially at similar rates [33]. This is illustrated on the inset of figure 4 (a) where $\hat{a}_\phi(\tau)$ for $\tau \in [0, 2.5]$ is shown for 12 equally spaced trajectories in $\phi \in [0, 2\pi)$ as projections onto the local bases formed by orthogonalizing $\hat{V}_1^{S1}, \hat{V}_2^{S1}$, i.e.

$$e_1 = \langle \hat{a}_\phi(\tau), \hat{V}_{1,\perp}^{S1} \rangle, \quad e_2 = \langle \hat{a}_\phi(\tau), \hat{V}_{2,\perp}^{S1} \rangle. \quad (31)$$

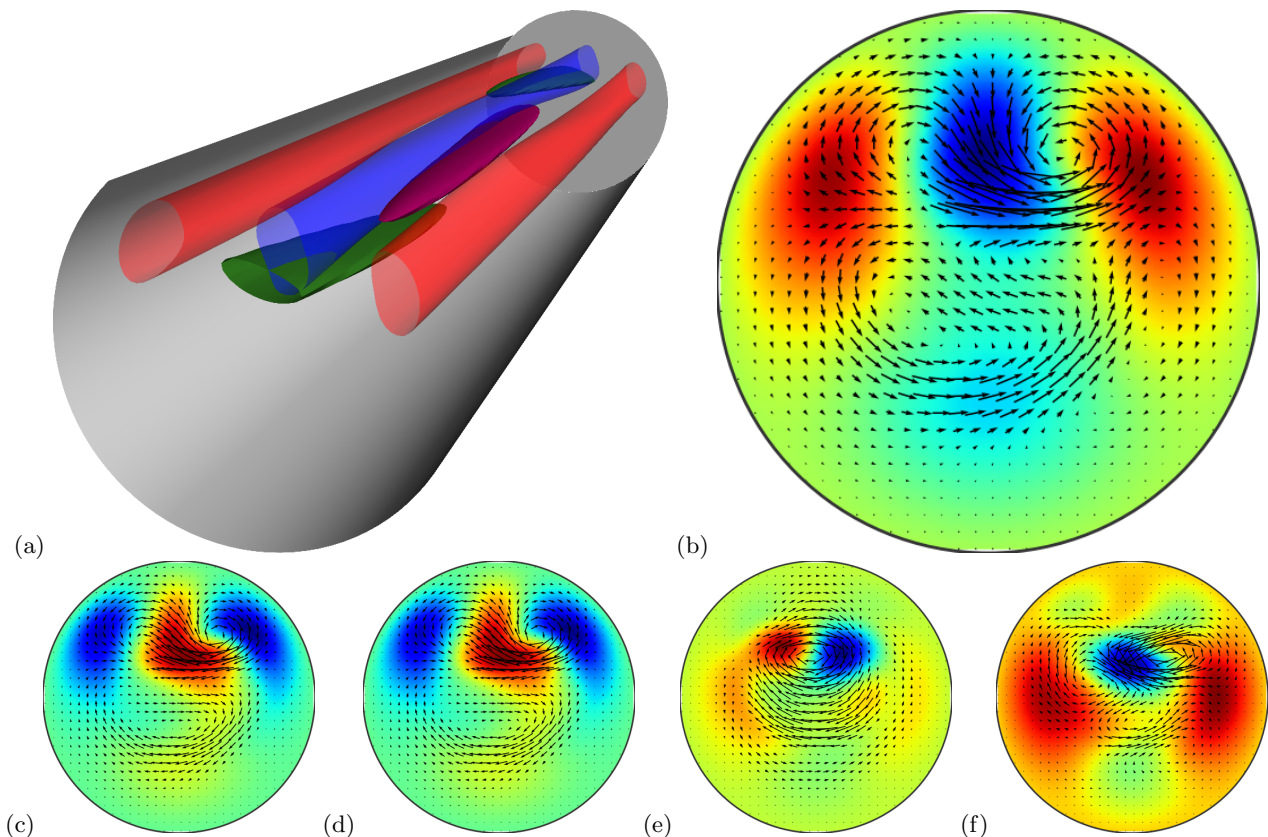


FIG. 3: (a) Isosurfaces of streamwise velocity at $u = 0.26$ (red) and $u = -0.33$ (blue) and streamwise vorticity at $\omega = \pm 0.40$ (green/purple) for the travelling wave S1 in three dimensions. Color-coded streamwise velocity and cross-stream velocity (arrows) averaged over half pipe-length $z \in (0, L/2]$ for S1 (b), and the unstable eigenvectors V_1^{S1} (c), \hat{V}_1^{S1} (d), V_2^{S1} (e), \hat{V}_2^{S1} (f). Flow direction into the page.

In (31), subscript \perp indicates that $\hat{V}_1^{S1}, \hat{V}_2^{S1}$ are orthonormalized via the Gram-Schmidt procedure; and the inset of figure 4 (a) illustrates that these bases capture local dynamics very well. Outer panel of figure 4 shows these trajectories for longer times, until they either become turbulent or laminarize. The trajectories that become turbulent or relaminarize are respectively colored pink and gray. While the projections are locally reliable, they fail to fully capture the dynamics away from S1 since the trajectories seem to fold onto themselves. In order to illustrate the qualitative features of the transition, we marked 3 instances on $\hat{u}_\pi(\tau)$ at $\tau \in [40, 60, 90]$ and visualized the corresponding three-dimensional flow structures on figure 4 (b, c, d). Note that the structures on figure 4 (b) are quite similar to those of S1, while the isosurface levels are set to higher values. This illustrates the first part of the transition: As the trajectory moves from S1 towards turbulence, streaks and vortices are amplified while their overall shape is more or less unchanged. As can be seen on figure 4 (c), this initial amplification is followed by the breakdown of streaks, and eventual turbulence (d) no longer exhibits structures that are coherent throughout the computational domain.

While the 12-trajectory approximation to the 2-dimensional unstable manifold is initially successful and illustrates the general features of the unstable manifold, such as relaminarization and transition to turbulence. It is clear from figure 4(a) that this approximation very quickly fails to cover the extend of the manifold that stays in the laminar-turbulent boundary. In order to uncover details of this part, we bisected between trajectories that transition to turbulence or relaminarize by changing ϕ in (30) until reaching the limit of numerical precision, as done in [6]. Differently, however, we enforced shift-and-reflect invariance in the time-stepping, in order to avoid numerical errors that could take trajectories outside the invariant subspace. In order to improve visibility, we visualized the unstable manifold approximated this way in three dimensions, using the least contracting stability eigenvector $\hat{V}_{4,1}^{S1}$ (symmetry reduced and orthonormalized) in addition to the leading-two (31) as the third basis. The unstable manifold visualized this way is shown in figure 5(a), where we coloured trajectories that eventually laminarize gray, and those that transition to turbulence pink. Additionally, we plotted the last four trajectories in the bisection procedure thicker than the rest, using colors red, blue, green, and black. For comparison, time series of the kinetic energy for these four trajectories is shown in figure 5(b), where we see that the trajectories stay on the ‘edge’ longer than 300 time units.

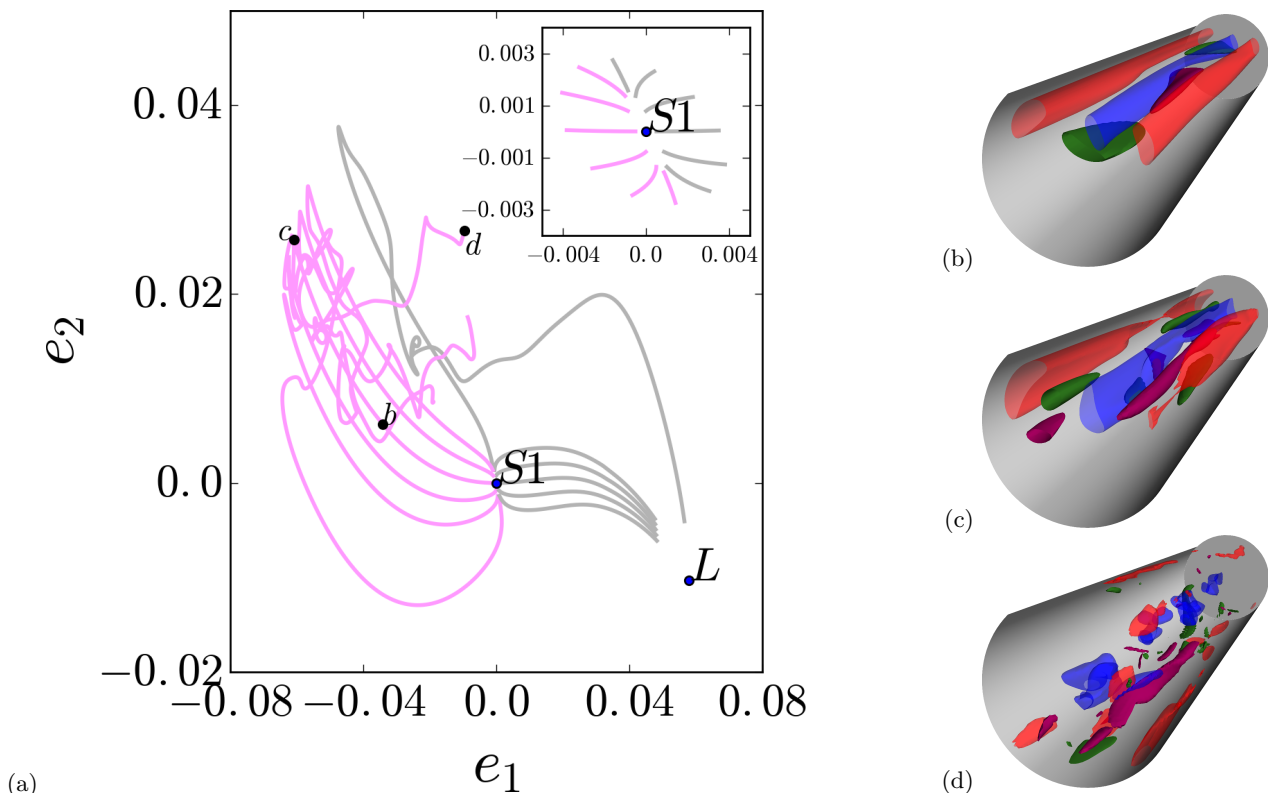


FIG. 4: (a) First approximation to the unstable manifold of $S1$, as forward-integrated trajectories with initial conditions (30) visualized as projections onto the local coordinate frame (31). L : Laminar solution. Inset: Same 12 trajectories on the unstable manifold for time interval $\tau \in [0, 2.5]$, illustrating the initial almost uniform expansion. Isosurfaces of streamwise velocity and vorticity at (b) $u = 0.36$ (red), $u = -0.50$ (blue), $\omega = \pm 0.99$ (green/purple), (c) $u = 0.50$ (red), $u = -0.62$ (blue) $\omega = \pm 1.5$ (green/purple), (d) $u = 0.66$ (red), $u = -0.71$ (blue) $\omega = \pm 9.0$ (green/purple). Flow direction into the page.

Upon our investigation of the trajectories that stay on the edge for the longest times, we observed episodes where state space trajectories slow down, which might indicate visits to the neighborhoods of other traveling waves. In order to quantify this, we measured the “self-recurrence”, which we defined as the norm of the difference between the symmetry-reduced states at time τ and $\tau - 5$ on the same trajectory. Note that in the symmetry-reduced state-space, the traveling waves are equilibria thus no extra care for the translation symmetry is necessary. Figure 6 shows the self-recurrence (a) over the trajectory which is shown blue on figure 5 and flow structures at different times on this trajectory (b-e).

As the trajectory evolves on the edge, it visits states with qualitatively different features: At the first minimum (figure 6 (c)) of the self-recurrence function, new fast streaks begin to form on the down-side of the pipe cross-section and at the second minimum (figure 6 (d)) initial fast streaks begin to disappear. Eventual transition to turbulence (figure 5 (e)) has quantitative features similar to those illustrated in figure 4: streaks amplify, spread, and break into smaller scale structures on the opposite side of the pipe. Newton-Krylov-hookstep searches starting from initial conditions visualized on figure 6 (c) and (d) converged to traveling wave solutions: Starting from the latter, we find $S1$, rotated by π about the pipe axis; whereas the Newton search starting from figure 6 (c) lead us to a previously unknown traveling wave, which we study in the next section.

B. Unstable manifold of $S1N$

Figure 7(a,b) shows three- and two-dimensional visualizations of the new solution, which we hereafter refer to as $S1N$. While being on the laminar-turbulent boundary, $S1N$ has a much more complicated structure compared to $S1$; its kinetic energy is roughly twice of it; and it has many more unstable directions. Solutions with similar properties were known [2, 4, 6, 22], mostly with higher azimuthal symmetries. However, none of the previously known solutions’ relevance to the full problem (without imposed symmetries) were established. Similarities between the initial condition’s figure 6 (c) and the converged state’s flow structures figure 7 (b) are apparent. Note particularly

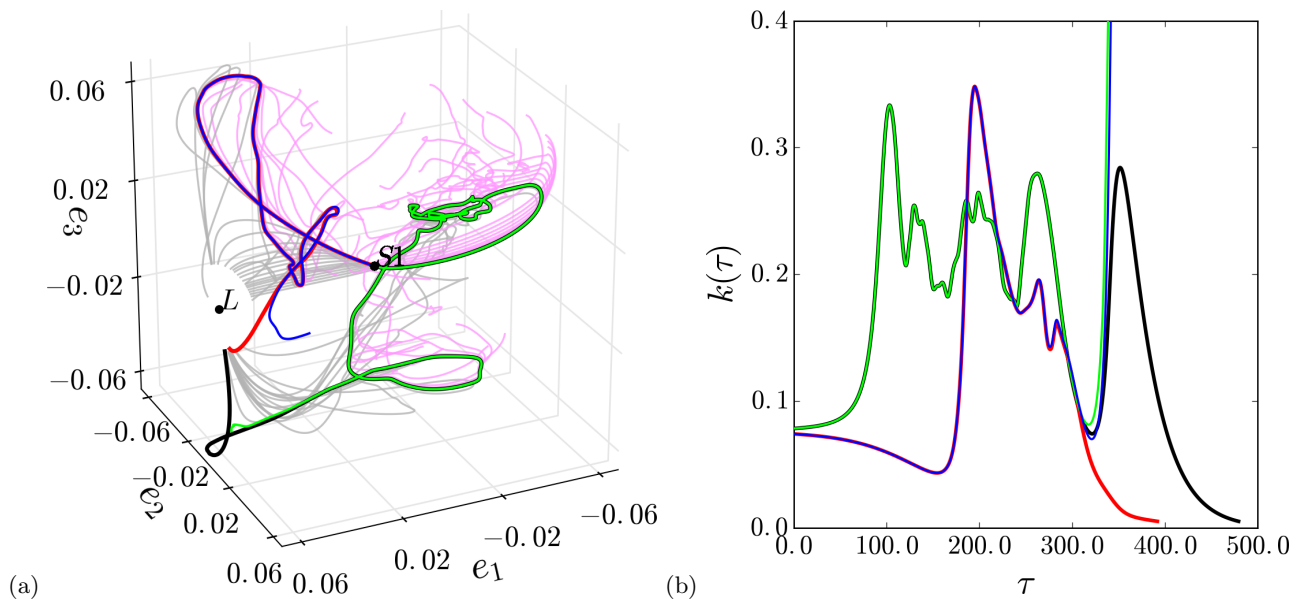


FIG. 5: (a) Unstable manifold of S1 approximated by bisecting between trajectories that relaminarize and those that develop into turbulence. (b) Time-series of kinetic energy for trajectories that stay on the edge for longest times.

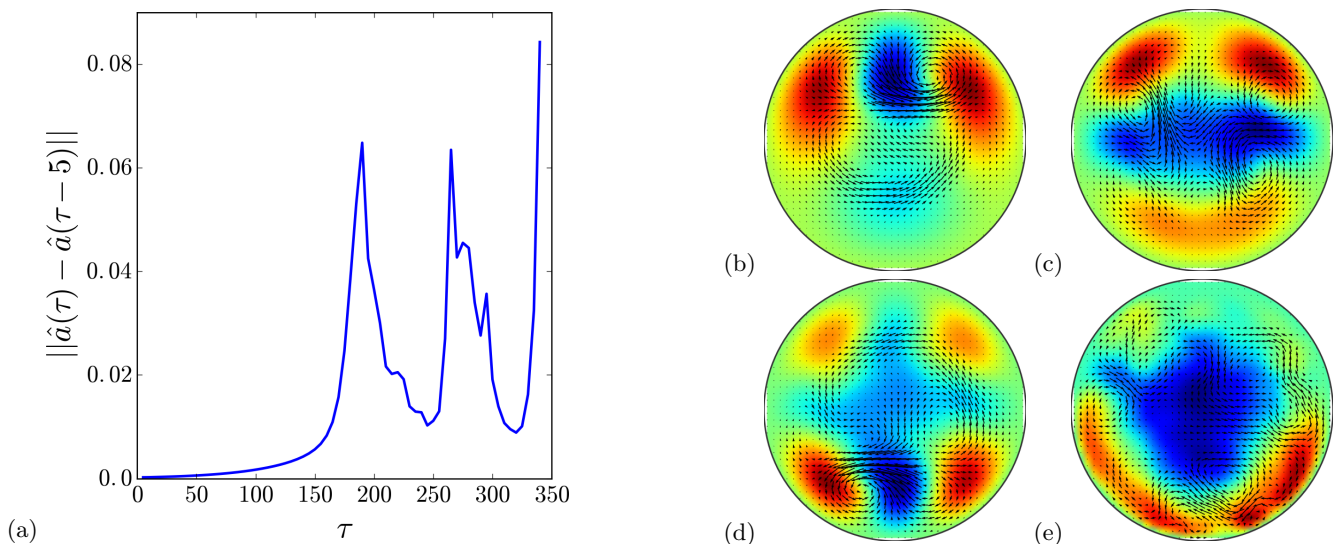


FIG. 6: (a) Self-recurrence measured over an edge trajectory (drawn blue in figure 5) on the unstable manifold of S1. Color-coded (fast/slow:red/blue) stream-wise velocity and cross-sectional velocity (arrows) averaged over half pipe length ($z \in [0, L/2]$) at (b) initial time $\tau = 0$, (c) local minimum $\tau = 245$, (d) local minimum $\tau = 320$, (e) final time $\tau = 345$. Flow direction into the page.

the locations of the vortical structures, which align very well. Since these structures do not extend along the pipe axis like streaks do, their one-to-one comparison is made possible by reduction to the translation-reduced state space (14).

As shown in figure 7 (c), S1N's unstable manifold is 11-dimensional in the shift-and-reflect subspace and more unstable eigenvalues were found when the symmetry restriction was lifted. This renders a complete computational study of its unstable manifold impractical. Therefore on figure 8, we visualize two-dimensional sub-manifolds associated with the leading three unstable eigenvalues in the full state-space as the first application of symmetry reduction in both z and θ .

Let $\lambda_k^{\text{S1N}} = \mu_k^{\text{S1N}} + i\omega_k^{\text{S1N}}$ and $V_k^{\text{S1N}} = U_k^{\text{S1N}} + iW_k^{\text{S1N}}$ respectively be complex eigenvalues and eigenvectors of S1N. Set of trajectories that approximately covers the linearized dynamics in the local two-dimensional plane spanned by

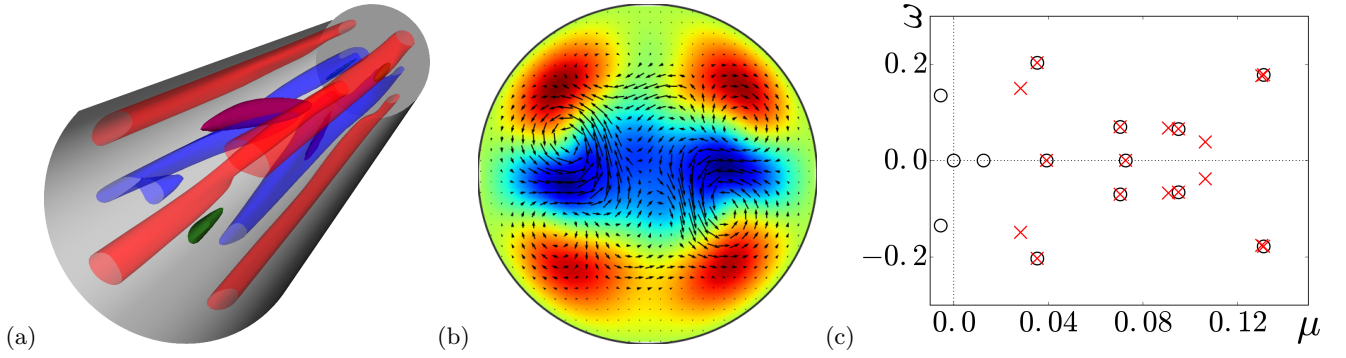


FIG. 7: (a) Isosurfaces of streamwise velocity at $u = 0.27 / -0.38$ (red / blue) and streamwise vorticity at $\omega_z = \pm 0.96$ (green / purple) of S1N. (b) Color-coded (fast/slow:red/blue) streamwise velocity and cross-sectional velocity (arrows) averaged over half pipe-length ($z \in [0, L/2]$) visualization of S1N. (c) Leading linear stability eigenvalues of S1N on complex plane computed in shift-and-reflect invariant subspace (black circles) and full state-space (red crosses).

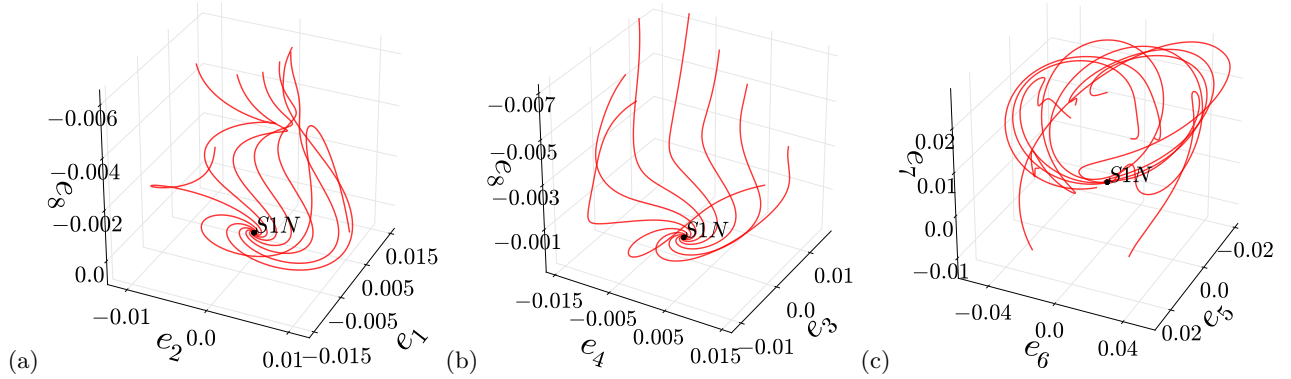


FIG. 8: Two-dimensional submanifolds associated with leading three unstable eigenvector of S1N approximated as set of trajectories with initial conditions given by (32) for $k = 1, 3, 5$ (a, b, c).

$(U_k^{\text{S1N}}, W_k^{\text{S1N}})$ are given by

$$\tilde{a}_\delta(\tau = 0) = \tilde{a}_{\text{S1N}} + \epsilon \exp(2\pi\mu_k^{\text{S1N}}\delta/\omega_k^{\text{S1N}})\tilde{U}_k^{\text{S1N}}, \text{ where } \delta \in [0, 1). \quad (32)$$

In (32), ϵ is a small number and $\tilde{\cdot}$ implies that state space points and eigenvectors are transformed into the first Fourier mode slice via (17) and (22) respectively. Under the linearized dynamics, a small perturbation to \tilde{a}_{S1N} in \tilde{U}_k direction expands by $\exp(2\pi\mu_k^{\text{S1N}}/\omega_k^{\text{S1N}})$ at one return of the spiral. Thus, the trajectories starting from the initial conditions (32) approximately satisfy $\tilde{a}_{\delta=0}(2\pi/\omega_k^{\text{S1N}}) = \tilde{a}_{\delta=1}(0)$, covering the associated two-dimensional submanifold. Using this approximation, we visualized time-forward dynamics of $2D$ -submanifolds associated with $V_{1,2}^{\text{S1N}}$, $V_{3,4}^{\text{S1N}}$, and $V_{5,6}^{\text{S1N}}$ on figure 8 (a, b, c) respectively. We assume that the eigenvalues are ordered from most unstable to the least i.e. $\text{Re } \lambda_1^{\text{S1N}} \geq \text{Re } \lambda_2^{\text{S1N}} \geq \text{Re } \lambda_3^{\text{S1N}} \geq \dots$. Note that complex eigenvalues and eigenvectors satisfy $\lambda_1^{\text{S1N}} = \lambda_2^{\text{S1N}*}$, $\lambda_3^{\text{S1N}} = \lambda_4^{\text{S1N}*}$, $\lambda_5^{\text{S1N}} = \lambda_6^{\text{S1N}*}$, $V_1^{\text{S1N}} = V_2^{\text{S1N}*}$, $V_3^{\text{S1N}} = V_4^{\text{S1N}*}$, $V_5^{\text{S1N}} = V_6^{\text{S1N}*}$, where $*$ stands for complex conjugation. Projection bases $\mathbf{e}_{1,2}$, $\mathbf{e}_{3,4}$, $\mathbf{e}_{5,6}$ are generated from \tilde{V}_1^{S1N} , \tilde{V}_3^{S1N} , and \tilde{V}_5^{S1N} as follows: By definition, $\tilde{V}_k^{\text{S1N}} = e^{i\phi}\tilde{V}_k^{\text{S1N}}$ is a stability eigenvector with eigenvalue λ_k^{S1N} . If we choose

$$\phi = \frac{1}{2} \arctan \frac{2 \langle \tilde{U}_k^{\text{S1N}}, \tilde{W}_k^{\text{S1N}} \rangle}{\|\tilde{W}_k^{\text{S1N}}\|^2 - \|\tilde{U}_k^{\text{S1N}}\|^2}, \quad (33)$$

$\tilde{U}_k^{\text{S1N}} = \text{Re } \tilde{V}_k^{\text{S1N}}$ and $\tilde{W}_k^{\text{S1N}} = \text{Im } \tilde{V}_k^{\text{S1N}}$ become orthogonal i.e. $\langle \tilde{U}_k^{\text{S1N}}, \tilde{W}_k^{\text{S1N}} \rangle = 0$. Projection bases are formed from these vectors as $(\mathbf{e}_k, \mathbf{e}_{k+1}) = (\tilde{U}_k^{\text{S1N}}/\|\tilde{U}_k^{\text{S1N}}\|, \tilde{W}_k^{\text{S1N}}/\|\tilde{W}_k^{\text{S1N}}\|)$ for $k = 1, 3, 5$. These bases fully capture local two-dimensional dynamics. We chose the third projection direction by trial and error to capture as much as possible as the trajectories develop into turbulence: $\mathbf{e}_7 = \tilde{V}_{11}^{\text{S1N}}/\|\tilde{V}_{11}^{\text{S1N}}\|$ and $\mathbf{e}_8 = \tilde{V}_1^{\text{S1N}}/\|\tilde{V}_1^{\text{S1N}}\|$. $\tilde{V}_{11}^{\text{S1N}}$ is the real unstable eigenvector of S1N with largest real eigenvalue $\lambda_{11}^{\text{S1N}}$ and \tilde{V}_1^{S1N} is the leading eigenvector of S1. We have already

illustrated in section III B that the V_1^{S1} direction corresponds to the trajectories in the vicinity of S1, which either laminarize or become turbulent and we are going to demonstrate that V_{11}^{S1N} takes the same role for S1N.

`Openpipeflow` normalizes stability eigenvectors such that their norms are equal to that of the associated solution, i.e. $\|V_k^{TW}\| = \|a_{TW}\|$. For computations of figure 8, we set $\epsilon = 10^{-4}$ (a, b) and $\epsilon = 10^{-8}$ (c); and picked 8 equidistant point in $[0, 1]$ for δ . While the spiral-out dynamics is clearly visible on figure 8 (a) and (b), trajectories look less organized on panel (c). This is because the imaginary part of the fifth eigenvalue $\lambda_5^{S1N} = 0.106 + i0.0383$ is rather small, rendering the time for the trajectories to complete a full spiral long. This is not the case for $\lambda_1^{S1N} = 0.131 + i0.178$ and $\lambda_3^{S1N} = 0.130 + i0.176$. While we might have obtained a better representation of the 2D manifold in figure 8(c) if we had used more trajectories to represent it, we chose to leave it as it is in order to illustrate the possible shortcomings of the method. All trajectories in figure 8 eventually become turbulent, illustrating the rich dynamics that the laminar-turbulent boundary can exhibit.

In the full state-space, the leading 10 stability eigenvalues of S1N are complex conjugate (figure 7 (c)) and $\lambda_{11}^{S1N} = 0.0727$ is purely real. In Figure 9 (a), we show the time-evolution of the kinetic energy when S1N is perturbed in the $\pm V_{11}^{S1N}$ direction. As one would expect from a solution on the laminar-turbulent boundary, the flow relaminarizes in one direction while becoming turbulent in the opposite. While this observation clearly shows that S1N also belongs to the laminar-turbulent boundary, whether or not its presence influences generic edge trajectories is not known. In the next section, we investigate this through a numerical experiment.

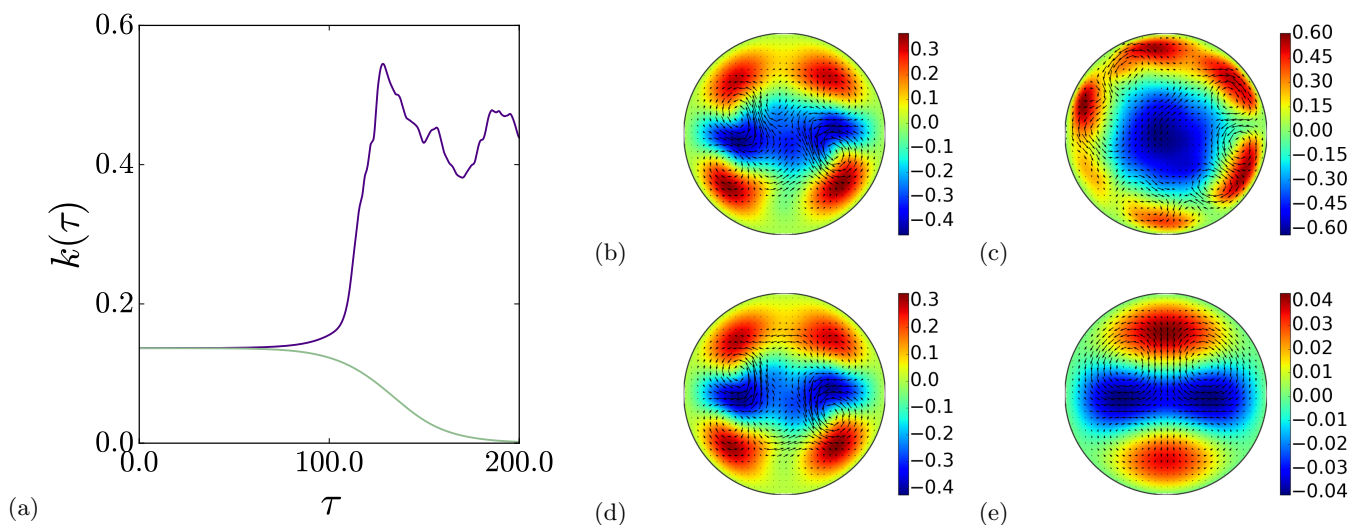


FIG. 9: (a) Time evolution of kinetic energy for trajectories starting from $a_{S1N} \pm 10^{-4} V_{11}^{S1N}$ (green/purple). (b, c, d, e) Color-coded stream-wise velocity and cross-sectional velocity (arrows) averaged over half pipe-length ($z \in [0, L/2]$) at times $\tau = 100, 200$ respectively on left and right. (b, c) Transition to turbulence (purple on panel a). (d, e) Laminarization (green on panel a).

C. Approaches to the traveling waves

In order to illustrate how a generic trajectory on the laminar-turbulent is influenced by the traveling wave solutions present in the edge state, we carried out an edge tracking [9, 34] experiment where we bisected between initial conditions that become turbulent and those that laminarize. For this purpose, we randomly took a typical turbulent state at $Re = 10000$, scaled this field down by constants $c = 0.5$ and $c = 0.75$ and used these states as initial conditions at $Re = 3000$. After observing that the former uneventfully proceeds towards the laminar solution while the latter triggers turbulence, we began generating new initial conditions by bisecting in c until we reached the limit of our numerical precision, such that the resulting trajectories stay in the laminar-turbulent boundary for longer and longer times. Kinetic energy time-series of these trajectories are shown in figure 10 (a). Such initial conditions are expected to approach to the invariant edge state [5] irrespective of how the very first state is generated. Therefore our choice of initial state from $Re = 10000$ is arbitrary and many other initial states would approach to the edge state following the same algorithm.

For every trajectory we generated through edge-tracking we the sampled flow states at intervals of $\Delta\tau = 5$ and brought these states to the first Fourier mode slice through (17). We then measured distances of these states from S1

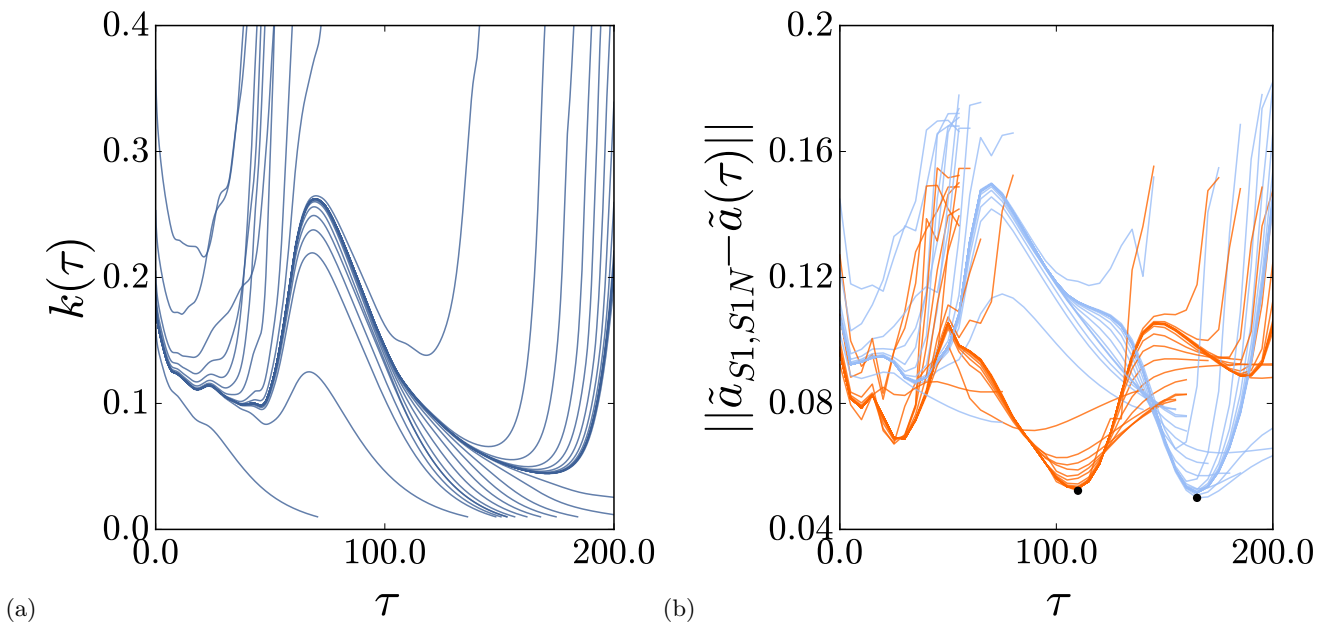


FIG. 10: (a) Time evolution of turbulent kinetic energy for edge tracking trajectories obtained through bisection. (b) Distance of bisection trajectories from S1 (blue) and S1N (orange). Minima of distances at $\tau = 110$ ($\min \|\tilde{a}_{S1N} - \tilde{a}(\tau)\|$) and at $\tau = 165$ ($\min \|\tilde{a}_{S1} - \tilde{a}(\tau)\|$) are marked black.

and S1N within the first Fourier mode slice. L_2 -distances of edge tracking trajectories from S1 and S1N are shown blue and orange respectively in figure 10(b), where each set of curves have a clear minimum marked with a black dot. We visualized these closest approaches next to the traveling waves they approach to in figure 11. Similarities between the flow structures of the traveling waves and the edge trajectories near them are clear, although the correspondence is not one-to-one.

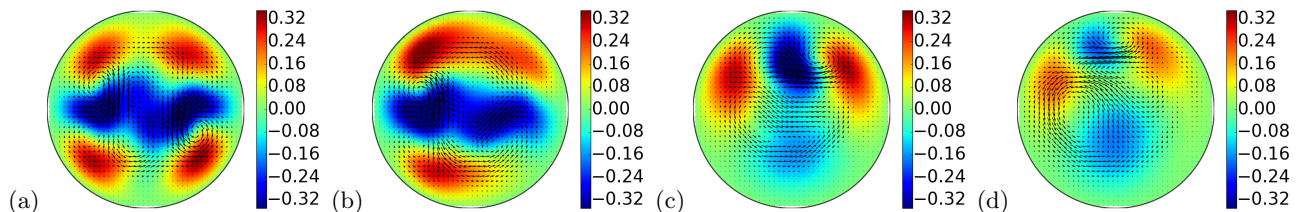


FIG. 11: Color-coded streamwise velocity and cross-sectional velocity (arrows) averaged over half-pipe length ($z \in [0, L/2]$) of (a) S1N, (b) closest approach of the trajectory on the edge to S1N at $\tau = 110$, (c) S1, (d) closest approach of the trajectory on the edge to S1 at $\tau = 165$. Each figure uses a fixed color-scale (\min, \max) = $(-0.35, 0.35)$.

Notice that without the symmetry-reduction, such an analysis would have required an optimization over axial translations and azimuthal rotations for each step in order to minimize the distance between two states. Symmetry-reduction eliminates this step, decreasing the computational cost of the analysis tremendously.

IV. CONCLUSION AND OUTLOOK

In this paper, we introduced a representation of the pipe flow, where the continuous symmetries in axial and azimuthal directions are simultaneously reduced. This technical step was a straightforward extension of the first Fourier mode slice implementation of ref. [20]. Nevertheless, it was not implemented before and it successfully closes the continuous symmetry reduction problem for pipe flow. Adapting this method to other canonical shear flows is straightforward. For instance, in a channel geometry, the role of axial and azimuthal coordinates are taken over by streamwise and spanwise coordinates; and one should only make a choice for the wall-normal dependence of the template functions. Since this choice is somewhat arbitrary, a convenient option could be the first Chebyshev polynomial that is often used for numerical discretization in this direction.

For the application, we decided to revisit the laminar-turbulent boundary in a short ($L \approx 5$) periodic computational cell of the pipe flow. Our first calculation that approximated the unstable manifold of S1 was very similar to that of Duguet *et al.* [6], who conjectured that the unstable manifold of S1 reached the neighborhoods of its own azimuthally rotated copies when it is followed along the laminar-turbulent boundary. Differently from ref. [6], we restricted our computation of the unstable manifold into the shift-and-reflect invariant subspace, to which the unstable manifold belongs. In addition, we visualized the unstable manifold as low-dimensional projections from the first Fourier mode slice (14). We found numerical evidence that the portion of this unstable manifold that is confined in the laminar-turbulent boundary visits the neighborhood of a new traveling wave, which we named S1N. Linear stability spectrum figure 7(c) showed that S1N has a very high dimensional unstable manifold, albeit being on the laminar-turbulent boundary. By visualizing two-dimensional submanifolds associated with leading three complex conjugate unstable eigenvectors on figure 7, we illustrated variety of paths from the edge state leading to the turbulence. Besides demonstrating the utility of the symmetry reduction in both z and θ , this computation also shows how rich the dynamics on the laminar-turbulent boundary can be. One main message we would like to deliver with the aid of these illustrations is that the asymptotic dynamics on the laminar-turbulent boundary in pipe flow should not be treated as a single state; but the edge state contains different regions with qualitatively different dynamics dictated by the nearby invariant solutions.

Both traveling waves we studied in this paper belonged to the shift-and-reflect invariant subspace of the pipe flow. One might argue against their relevance for the dynamics in the laminar-turbulent boundary since generic trajectories live in the full state space. Cvitanović *et al.* [35] nicely illustrates for one-dimensional Kuramoto-Sivashinsky system that the unstable manifolds of equilibrium solutions, all of which belong to the reflection invariant subspace, successfully captures the qualitative dynamics in the full state space of the $O(2)$ -equivariant system. Our case here is similar to theirs since the symmetry in the azimuthal direction is also $O(2)$. Therefore, it is quite reasonable to expect for S1's unstable manifold to form the backbone of the asymptotic dynamics on the laminar-turbulent boundary, given all the evidence that the edge state is located in its vicinity. Indeed, visualizations of figure 11 clearly show the similarities between the full state space trajectories and the traveling waves nearby.

Recently, Suri *et al.* [36] studied the weekly turbulent quasi-two-dimensional flow in laboratory experimentally and numerically. They demonstrated that when a turbulent trajectory comes close to an equilibrium, it leaves this neighborhood by following the unstable manifold of the solution. The tools we presented here, in particular, the methods for approximating and visualizing the unstable manifolds after symmetry-reduction, pave the way for a similar analysis in three-dimensional pressure-driven flows, which have traveling wave solutions rather than equilibria.

As we have shown in section III C, symmetry-reduction frees us from reduced metrics, such as energy input or dissipation, that do not carry all information of the state space, and allows for measuring distances in the full state space. However, one should always keep in mind that two points that are at a short distance in the state space of a nonlinear system might evolve towards completely different regions. In order to conclusively answer whether or not a state space trajectory is “guided” by a particular unstable manifold, we should measure distances between curves in the state space, rather than points. While the finite-dimensional projections such as figures 4, 5, and 8 serve this purpose, they do not provide a complete picture of the infinite-dimensional state space. We believe developing computationally feasible methods for comparing shapes in high-dimensional state spaces is an important future problem for turbulence studies.

Acknowledgments

We would like to acknowledge stimulating discussions with Yohann Duguet and Predrag Cvitanović. This research was supported in part by the National Science Foundation under Grant No. NSF PHY11-25915.

-
- [1] A. Meseguer and L. N. Trefethen, *J. Comput. Phys.* **186**, 178 (2003).
 - [2] H. Faisst and B. Eckhardt, *Phys. Rev. Lett.* **91**, 224502 (2003).
 - [3] C. C. T. Pringle and R. R. Kerswell, *Phys. Rev. Lett.* **99**, 074502 (2007).
 - [4] C. C. T. Pringle, Y. Duguet, and R. R. Kerswell, *Phil. Trans. Royal Soc. A* **367**, 457 (2009), [arXiv:0804.4854](https://arxiv.org/abs/0804.4854).
 - [5] T. M. Schneider, B. Eckhardt, and J. Yorke, *Phys. Rev. Lett.* **99**, 034502 (2007).
 - [6] Y. Duguet, A. P. Willis, and R. R. Kerswell, *J. Fluid Mech.* **613**, 255 (2008), [arXiv:0711.2175](https://arxiv.org/abs/0711.2175).
 - [7] F. Mellibovsky, A. Meseguer, T. M. Schneider, and B. Eckhardt, *Phys. Rev. Lett.* **103**, 054502 (2009), URL <https://link.aps.org/doi/10.1103/PhysRevLett.103.054502>.
 - [8] E. Hopf, *Commun. Pure Appl. Math.* **1**, 303 (1948).
 - [9] T. Itano and S. Toh, *J. Phys. Soc. Japan* **70**, 701 (2001).

- [10] S. Toh and T. Itano, *J. Fluid Mech.* **481**, 67 (2003).
- [11] T. M. Schneider, J. F. Gibson, M. Lagha, F. D. Lillo, and B. Eckhardt, *Phys. Rev. E* **78**, 037301 (2008), [arXiv:0805.1015](#).
- [12] T. M. Schneider, D. Marinc, and B. Eckhardt, *J. Fluid Mech.* **646**, 441 (2010).
- [13] S. Zammert and B. Eckhardt, *PAMM* **14**, 591 (2014).
- [14] T. Khapko, T. Kreilos, P. Schlatter, Y. Duguet, B. Eckhardt, and D. S. Henningson, *J. Fluid Mech.* **801** (2016).
- [15] P. Cvitanović, R. Artuso, R. Mainieri, G. Tanner, and G. Vattay, *Chaos: Classical and Quantum* (Niels Bohr Inst., Copenhagen, 2015), [ChaosBook.org](#).
- [16] G. Kawahara and S. Kida, *J. Fluid Mech.* **449**, 291 (2001).
- [17] D. Viswanath, *J. Fluid Mech.* **580**, 339 (2007), [arXiv:physics/0604062](#).
- [18] P. Ritter, F. Mellibovsky, and M. Avila, *New J. Phys.* **18**, 083031 (2016).
- [19] J. F. Gibson, J. Halcrow, and P. Cvitanović, *J. Fluid Mech.* **611**, 107 (2008), [arXiv:0705.3957](#).
- [20] N. B. Budanur and B. Hof, *J. Fluid Mech* **827**, R1 (2017).
- [21] A. P. Willis, *SoftwareX* **6**, 124 (2017), ISSN 2352-7110, URL <http://www.sciencedirect.com/science/article/pii/S2352711017300158>.
- [22] H. Wedin and R. R. Kerswell, *J. Fluid Mech.* **508**, 333 (2004).
- [23] N. B. Budanur, K. Y. Short, M. Farazmand, A. P. Willis, and P. Cvitanović, *J. Fluid Mech* **833**, 274 (2017), [arXiv:1705.03720](#).
- [24] A. P. Willis, P. Cvitanović, and M. Avila, *J. Fluid Mech.* **721**, 514 (2013), [arXiv:1203.3701](#).
- [25] N. B. Budanur, P. Cvitanović, R. L. Davidchack, and E. Siminos, *Phys. Rev. Lett.* **114**, 084102 (2015).
- [26] N. B. Budanur, D. Borrero-Echeverry, and P. Cvitanović, *Chaos* **25**, 073112 (2015), [arXiv:1411.3303](#).
- [27] S. Froehlich and P. Cvitanović, *Commun. Nonlinear Sci. Numer. Simul.* **17**, 2074 (2012), [arXiv:1101.3037](#).
- [28] P. Cvitanović, D. Borrero-Echeverry, K. Carroll, B. Robbins, and E. Siminos, *Chaos* **22**, 047506 (2012).
- [29] C. W. Rowley and J. E. Marsden, *Physica D* **142**, 1 (2000).
- [30] P. Chossat and R. Lauterbach, *Methods in Equivariant Bifurcations and Dynamical Systems* (World Scientific, Singapore, 2000), ISBN 978-981-02-3828-5.
- [31] D. Armbruster, J. Guckenheimer, and P. Holmes, *Physica D* **29**, 257 (1988).
- [32] A. de Lozar, F. Mellibovsky, M. Avila, and B. Hof, *Phys. Rev. Lett.* **108**, 214502 (2012).
- [33] B. Krauskopf, H. M. Osinga, E. J. Doedel, M. E. Henderson, J. Guckenheimer, A. Vladimirovsky, M. Dellnitz, and O. Junge, *Int. J. Bifurc. Chaos* **15**, 763 (2005), URL <http://www.worldscientific.com/doi/abs/10.1142/S0218127405012533>.
- [34] J. D. Skufca, J. A. Yorke, and B. Eckhardt, *Phys. Rev. Lett.* **96**, 174101 (2006).
- [35] P. Cvitanović, R. L. Davidchack, and E. Siminos, *SIAM J. Appl. Dyn. Syst.* **9**, 1 (2009), [arXiv:0709.2944](#).
- [36] B. Suri, J. Tithof, R. O. Grigoriev, and M. F. Schatz, *Phys. Rev. Lett.* **118**, 114501 (2017), [arXiv:1611.02226](#), URL <https://link.aps.org/doi/10.1103/PhysRevLett.118.114501>.